


Article

Spirobifluorene-Based D-A Type Conjugated Polymer Photocatalysts for Water Splitting

Hao Zhao ^{1,*} , Pengyao Sun ², Hui Xu ², Xinyi Xiao ¹, Zhiyuan Kong ¹, Shige Song ¹, Weihao Li ¹, Luzun Liu ¹, Jiadong Wang ¹ and Xiaobo Pan ^{2,*}

¹ School of Physics and Electronic Information, Yantai University, Yantai 264005, China; xiaoxinyi@y.tu.edu.cn (X.X.); kongzhiyuan@y.tu.edu.cn (Z.K.); songshige@y.tu.edu.cn (S.S.); liweihao@y.tu.edu.cn (W.L.); liuluzun@y.tu.edu.cn (L.L.); wangjiadong@y.tu.edu.cn (J.W.)

² State Key Laboratory of Applied Organic Chemistry, College of Chemistry and Chemical Engineering, Lanzhou University, Lanzhou 730000, China; sunpengyao163@163.com (P.S.); njtuzi0407@163.com (H.X.)

* Correspondence: zhaohao@y.tu.edu.cn (H.Z.); boxb@lzu.edu.cn (X.P.)

Abstract: Exploring synthetic pathways for efficient photocatalysts has always been a major goal in catalysis. The performance of organic photocatalysts is affected by a variety of complex factors, and how to understand the structure–effect relationship is the key to designing efficient photocatalysts. This work explored the feasibility of constructing large-specific-surface-area conjugated microporous polymers (CMPs) based on stereoscopic units like spirobifluorene and achieving efficient photocatalytic activity by modulating the donor–acceptor (D-A) ratio with dibenzothiophene sulfone. Crosslinked pore structures were successfully constructed, and the specific surface area increased with the ratio of spirobifluorene. When the molar ratio of D-A was 1:20, polymer Spso-3 showed the highest photocatalytic hydrogen production activity, at 22.4 mmol h⁻¹ g⁻¹. The findings indicate that constructing D-A type CMPs should be a promising approach to improving the performance of photocatalytic water separation. The appropriate push–pull effect of the D-A structure promotes the photo-induced separation of electron–hole pairs, and the porous structure built on steric units offers ample space for catalytic reactions. This work could provide case references for structural design and the structure–effect relationship of efficient polymer photocatalysts.

Keywords: photocatalytic; conjugated polymer; D-A type; spirobifluorene; dibenzothiophene



Citation: Zhao, H.; Sun, P.; Xu, H.; Xiao, X.; Kong, Z.; Song, S.; Li, W.; Liu, L.; Wang, J.; Pan, X. Spirobifluorene-Based D-A Type Conjugated Polymer Photocatalysts for Water Splitting. *Catalysts* **2024**, *14*, 717. <https://doi.org/10.3390/catal14100717>

Academic Editor: Jae Sung Lee

Received: 26 September 2024

Revised: 10 October 2024

Accepted: 11 October 2024

Published: 14 October 2024



Copyright: © 2024 by the authors. Licensee MDPI, Basel, Switzerland. This article is an open access article distributed under the terms and conditions of the Creative Commons Attribution (CC BY) license (<https://creativecommons.org/licenses/by/4.0/>).

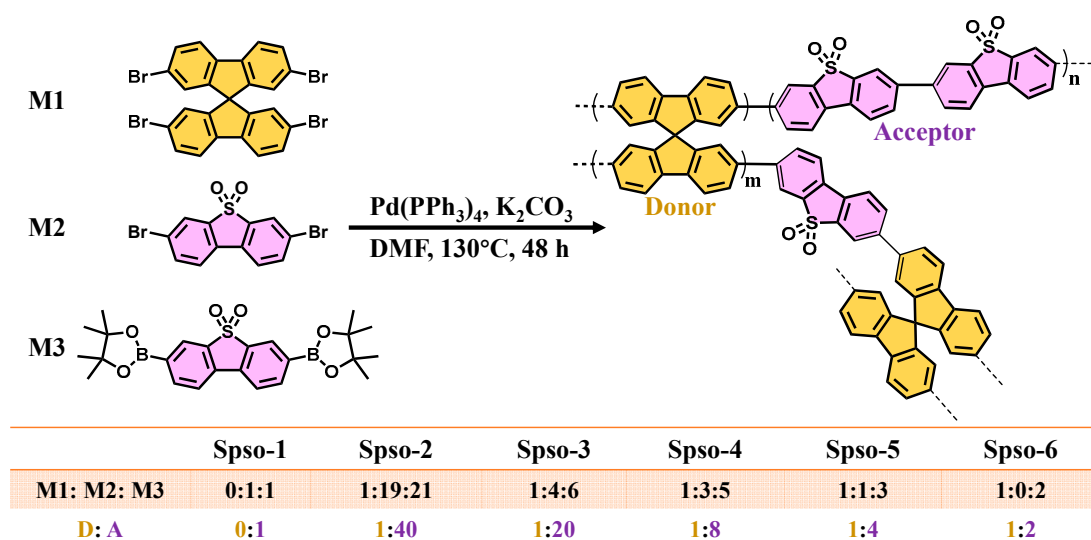
1. Introduction

Hydrogen, a secondary energy resource with a wide range of clean and carbon-free sources and rich application scenarios, is the ideal medium to substitute traditional fossil energy sources and support the large-scale development of renewable energy [1–3]. Using solar energy for direct photocatalysis-induced water decomposition for hydrogen production is a tempting and challenging energy conversion approach [4,5]. A 100 m² scale prototype photocatalytic solar hydrogen production system constructed by Domen has operated stably for many years and enables autonomous hydrogen recovery, further demonstrating the feasibility of large-scale photocatalytic hydrogen production in the future [6]. However, the lower hydrogen production efficiency is still the main challenge limiting the use of this solution in reality, and the development of efficient, inexpensive, and environmentally friendly photocatalyst materials has become a research focus in catalytic chemistry and energy chemistry [7].

In recent times, organic conjugated polymers have gained significant interest owing to their distinctive advantages. These encompass the capacity for tunable light absorption and electronic properties, the ease of modifying the skeletal architecture and porosity, superior light stability, and robust economic viability; they mainly include the family of g-C₃N₄ [8–11], linear conjugated polymers [12–15], conjugated microporous polymers (CMPs) [16–20], covalent organic frameworks (COFs) [21–23], and covalent triazine-based

frameworks (CTFs) [24–26]. However, the performance of polymer photocatalysts is affected by a variety of complex factors, and how to understand the structure–effect relationship is the key to designing efficient photocatalysts [20,27]. In our previous studies, the influence mechanisms of numerous parameters in organic photocatalysts were investigated, including the effect of bandgap modulation on the light absorption range, the effect of the donor–acceptor (D-A) structure and ratio on the separation efficiency of electron–hole pairs, and a preliminary mechanism for the promotion of the catalytic efficiency by strong dipole units like $B \leftarrow N$ [28–31]. It is very important to consider the interconnectivity of different factors, among which the optimization of the D-A ratio and the increment in specific surface area are beneficial for photocatalytic reactions. As a molecule with a tetragonal–disphenoid shape, spirobifluorene not only functions as tetrahedral nodes for three-dimensional structures to construct CMPs boasting a large specific surface area but also exhibits remarkable potential in optoelectronic devices on account of its distinctive conjugated structure [32–35]. Furthermore, the orthogonal conformation of two planar intermolecular fluorene units possesses significant rigidity and can enhance the stability of the resulting CMPs [36]. Building organic photocatalysts around spirobifluorene units would be expected for good photocatalytic performance.

Herein, this work attempted to realize large-specific-surface-area CMP photocatalysts using spirobifluorene as the core unit, matching a wide-bandgap dibenzothiophene sulfone electron acceptor to achieve D-A structure construction (Scheme 1), and developed conjugated polymer series with various strengths of push–pull electron effects by copolymerizing them in various proportions. Crosslinked pore structures were successfully constructed, and the specific surface area increased with the ratio of spirobifluorene. The highest photocatalytic hydrogen production activity of polymer Sps0-3, $22.4 \text{ mmol h}^{-1} \text{ g}^{-1}$, was observed when the molar ratio of D-A was 1:20, which could be attributed to the increase in the photo-induced carrier separation efficiency, suggesting that the photocatalytic performance is dependent on the molar ratio of D-A in the backbone. The molar ratio of D-A serves as a significant variable in achieving a balance between the separation and transport of photogenerated electrons and holes, further influencing the polymers' photocatalytic performance. All indications showed that the establishment of D-A type CMPs constitutes a useful approach to enhancing photocatalytic performance for water splitting. The conjugated D-A structure has the ability to facilitate the separation of light-induced electron–hole pairs. Meanwhile, the porous structure constructed on the basis of stereoscopic units offers ample space for catalytic reactions.



Scheme 1. Synthetic route of Sps0-1~Sps0-6.

2. Results and Discussion

2.1. Structure and Morphology Analyses

Six random polymers were prepared by adjusting the molar feed ratio of 2,2',7,7'-tetrabromo-9,9'-spirobifluorene, 3,7-dibromo-dibenzothiophene sulfone and 3,7-diborate-dibenzothiophene sulfone using Pd(0)-catalyzed Suzuki–Miyaura coupling polymerization (Scheme 1). The molar ratio of D-A in the polymer structure was controlled between 0:1 and 1:2. The D-A ratio of 0:1 represents the chain polymer of polydibenzothiophene sulfone, which is still named Spso-1 for uniformity, and the other CMPs were named Spso-2 to Spso-5. The polymers obtained were processed through Soxhlet extraction using tetrahydrofuran (THF) to eliminate unwanted impurities. No solubilizing side chains were incorporated into the polymer framework. Consequently, all the obtained polymers were insoluble in common organic solvents like methanol, hexanes, THF, acetone, and so on. This phenomenon might be attributed to the rigid backbone of the polymer, which further impedes the determination of its molecular weight.

The functional group structures of the six polymers were determined by Fourier transform infrared (FT-IR) spectroscopy. As shown in Figure 1a, the infrared spectra of all polymers showed the symmetric and asymmetric stretching vibration peaks of the O=S=O bond of the sulfone group at 1300 and 1155 cm^{-1} , as well as the stretching vibration peak of the aromatic ring $\text{C}=\text{C}$ at around 1600 cm^{-1} [37–39]. The presence of the sulfone group and aromatic ring in the polymers was confirmed by FT-IR spectroscopy. Since the photocatalytic water splitting reaction needs to be carried out under strong light irradiation, which must lead to an inevitable long-term temperature increase in the photoreactor, the polymers should be thermally stable [40]. The thermal stability of the polymers was studied by thermogravimetric analysis (TGA). The decomposition temperatures at which the polymer mass loss was 5% were 469 °C (Spso-1), 449.1 °C (Spso-2), 460.8 °C (Spso-3), 470.1 °C (Spso-4), 445.8 °C (Spso-5), and 441.6 °C (Spso-6), all above 400 °C, indicating that the introduction of spirobifluorene did not affect the thermal stability of the material (Figure 1b). In the low-temperature range below 430 °C, the weight loss was attributed to physically adsorbed water inside and outside the pores, pyrolysis of certain functional groups on the surface of the material, and volatilization of trace amounts of residual solvent [41]. All the polymers met the thermal stability requirements for the photocatalytic reaction. The powder X-ray diffraction (PXRD) patterns of the six conjugated polymers, Spso-1 to Spso-6, are shown in Figure 1c. Polymers Spso-1 to Spso-4 had a distinct sharp diffraction peak at around $2\theta = 12.7^\circ$ and 24.5° , respectively. The diffraction peak at around 24.5° indicated that the π - π stacking distance of the polymer skeleton was in the range of 3.8–4 Å. There was a low-intensity broad peak at around $2\theta = 21.8^\circ$. Polymers with a molar ratio of spirobifluorene to dibenzothiophene sulfone in the range of (0–1:8) had more distinct peaks, indicating that they had more crystalline structures, which was more conducive to the improvement of photocatalytic activity [42]. However, the PXRD patterns of polymers Spso-5 and Spso-6 did not show obvious diffraction peaks, only a low-intensity broad peak in the shape of a bun, indicating that the crystallinity of the polymers with a molar ratio of spirobifluorene to dibenzothiophene sulfone in the range of (1:4–1:2) was poor and they were amorphous. With the ratio increase in spirodifluorene in the polymer skeleton, the diffraction peak intensity varies from a peak with a certain intensity to a steamed bun-like large package peak, and the structure gradually changes from order to disorder, that is, from semi-crystalline to amorphous. The outcomes revealed that a higher proportion of spirobifluorene in the polymer skeleton would significantly reduce the crystallinity of the material, while a lower proportion of spirobifluorene had little effect on the crystallinity of the material. The unique rigid three-dimensional structure of spirobifluorene will produce a large spatial site resistance in the polymer. As the spirobifluorene ratio increases, the spatial site resistance effect becomes obvious, causing the alignment and regular stacking of polymer molecular chains to become difficult, and the freedom of molecular chains decreases, and the crystallization process is inhibited, which leads to a decrease in crystallinity [43–46]. The microscopic morphology of the polymer

has a significant influence on the photocatalytic activity [47]. By observing the microscopic morphology of the six polymers using a scanning electron microscope (SEM), as shown in Figure 1d, we observed that polymer Sps0-1 had an irregular flake-like morphology. When a small amount of spirobifluorene was introduced into the polymer skeleton, that is, when the ratio of spirobifluorene to dibenzothiophene sulfone was in the range of 1:40 to 1:8, polymers Sps0-2, Sps0-3, and Sps0-4 exhibited a thin flake-like morphology. With the further increase in the ratio of spirobifluorene to dibenzothiophene sulfone, polymers Sps0-5 and Sps0-6 exhibited an aggregated granular morphology. Results of SEM demonstrated that the variation in the D-A ratio changes the polymers' micromorphology, with a smaller ratio of spirobifluorene in the polymer backbone favoring the formation of flake-like morphology. Different morphologies of the photocatalyst would result in differences in the specific surface area and the number of reactive sites, thus having an important influence on the carrier transport and photocatalytic activity [48]. The nanosheet structure has better carrier transport efficiency than bulk materials [49,50].

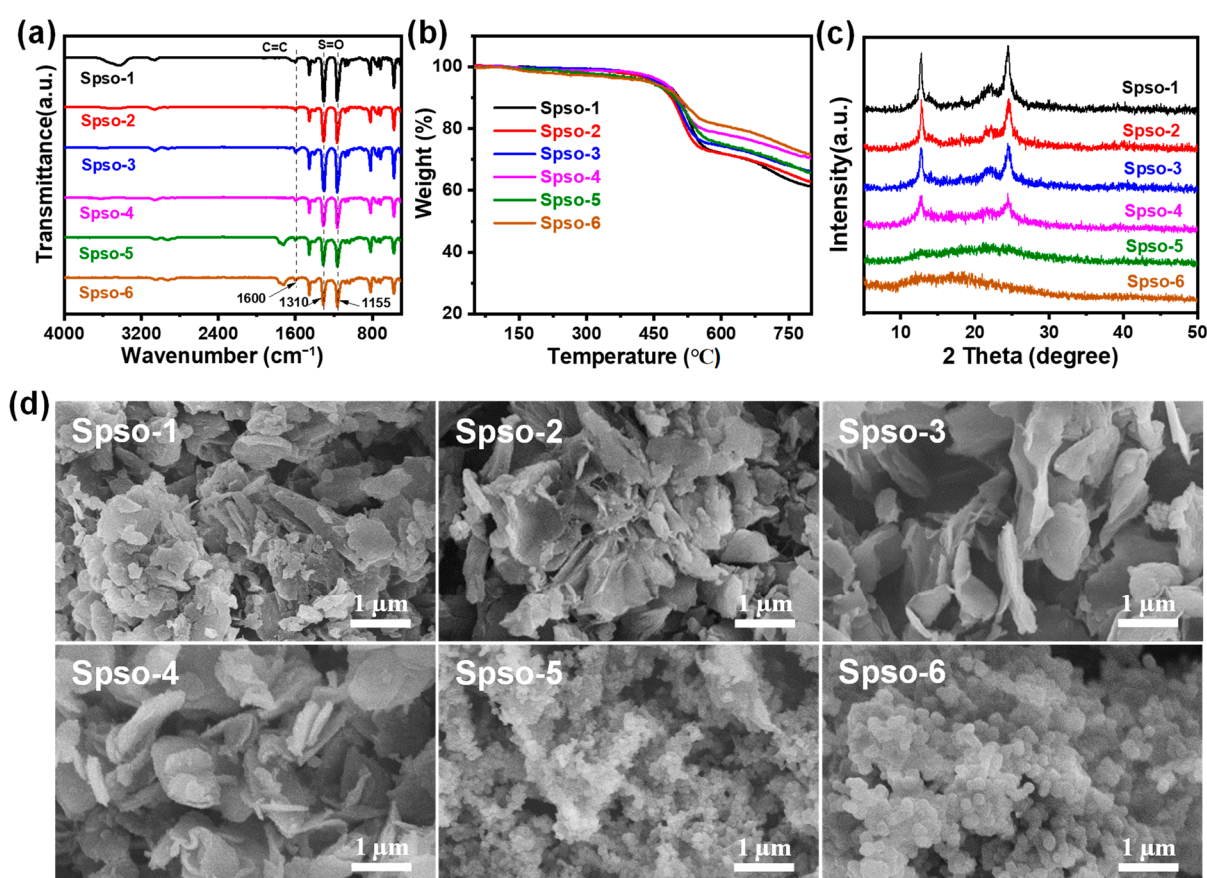


Figure 1. (a) FT-IR spectra of the polymers. (b) TGA traces for the polymers were measured under a nitrogen atmosphere. (c) PXRD patterns and (d) SEM images of all polymers.

2.2. Energy Band and Photophysical Property

The polymers Sps0-1~Sps0-6 showed almost no difference in color under natural light and were all yellow. Under the irradiation of a 365 nm UV lamp, the fluorescence color of the polymers shifted from yellow-green to blue-green, and a slight blue shift phenomenon occurred (Figure 2a). The blue shift in the polymer color could be attributed to the highly distorted structure of the spirobifluorene, which prevents the departure of electrons from the domain [51].

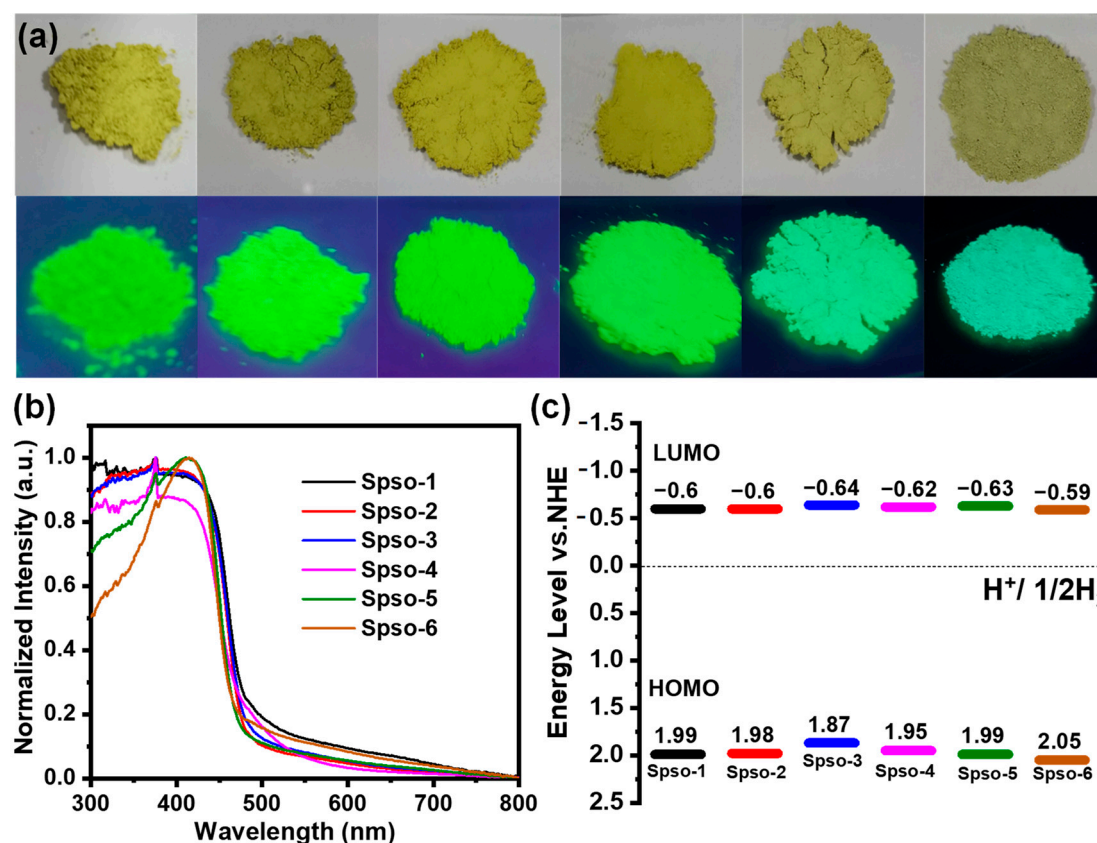


Figure 2. (a) Digital photographs of polymers in natural light (top) and 365 nm UV light (bottom). (b) UV-vis absorption spectra and (c) energy level diagrams of polymers.

The ability of the polymer to absorb light is an important element for achieving high-efficiency photocatalytic hydrogen production activity. The solid UV-visible diffuse reflectance spectra (DRS) showed a series of absorption edge bands, ranging from 469 to 495 nm (Figure 2b). The light absorption of all polymers extended to the visible light region. By analyzing the DRS spectra of the six polymers, the maximum absorption wavelengths of polymers Sps0-1 to Sps0-6 were 479 nm, 480 nm, 495 nm, 482 nm, 474 nm, and 469 nm, respectively. That is, with the increase in the spirobifluorene content in the polymer skeleton, the light absorption of the polymer did not change significantly. There was a slight red shift at first, and then a slight blue shift. From the light absorption edge band, we have the following formula [52]:

$$E_g = 1240/\lambda \quad (1)$$

The optical bandgaps of polymers Sps0-1 to Sps0-6 were 2.59 eV, 2.58 eV, 2.51 eV, 2.57 eV, 2.62 eV, and 2.64 eV, respectively, decreasing from 2.59 eV to 2.51 eV and then gradually increasing to 2.64 eV. Among the six polymers, Sps0-3 had the smallest bandgap, and Sps0-6 had the largest bandgap. Compared with polymer Sps0-1, Sps0-3 had a red shift of 16 nm, and Sps0-6 had a blue shift of 10 nm. These results indicated that changing the molar ratio of D-A in the conjugated polymer skeleton could fine-tune the light absorption ability of the polymer, thereby affecting the photocatalytic hydrogen evolution activity of the material. The Mott-Schottky curve was obtained by the Mott-Schottky method at an electrochemical workstation [53]. The intersection of the longest tangent line with the X-axis of curves is the flat band potential of the polymer. A positive slope of the curve indicates an n-type semiconductor and a negative slope indicates a p-type semiconductor. For n-type semiconductors, the flat band potential is negative 0.1–0.3 V compared to the

conduction band potential. The conductor position of the semiconductor is calculated according to the following formula:

$$E_{\text{LUMO}} (\text{NHE}) = E (\text{Ag}/\text{AgCl}) + 1.976 \text{ V} - 0.3\text{V} \quad (2)$$

Combined with UV-Vis absorption spectra, the corresponding valence band positions are obtained (Figure 2c and detailed energy level data in Table 1). The results show that the lowest unoccupied molecular orbital (LUMO) level of all polymers is above the reduction potential of water, which has enough driving force for proton reduction half-reaction. The LUMO energy level of the six polymers did not change significantly, indicating that changing the molar ratio of D-A did not have a significant effect on the energy level of the materials. The Brunauer–Emmett–Teller (BET) specific surface areas of the polymers were determined using nitrogen adsorption–desorption experiments. The specific surface areas of the six polymers, Spso-1~Spso-6, are listed in Table 1, at 54.3, 177.3, 131.8, 267.4, 384.8, and 681.7 $\text{m}^2 \text{g}^{-1}$, respectively. Due to the highly distorted spatial structure of spirodifluorene, increasing the ratio of spirodifluorene significantly improved the specific surface area of the materials. The specific surface area of the polymers generally shows an increasing trend, while the specific surface area of Spso-3 slightly decreases, which may be related to its unique lamellar structure.

Table 1. Energy level and specific surface area data of polymers.

Sample	λ_{onset} (nm)	λ_{em} (nm)	E_{g} (eV)	BET Specific Surface Area ($\text{m}^2 \text{g}^{-1}$)	LUMO (eV)	HOMO (eV)
Spso-1	479	511	2.59	54.3	−0.60	1.99
Spso-2	480	507	2.58	177.3	−0.60	1.98
Spso-3	495	505	2.51	131.8	−0.64	1.87
Spso-4	482	503	2.57	267.4	−0.62	1.95
Spso-5	474	492	2.62	384.8	−0.63	1.99
Spso-6	469	485	2.64	681.7	−0.59	2.05

The fluorescence emission peaks of Spso-1 to Spso-6 are 511 nm, 507 nm, 505 nm, 503 nm, 492 nm, and 485 nm, respectively, with a trend of gradual blue shift (Figure 3a), suggest that the photophysical properties and electronic structures of the polymers can be finely adjusted within a wide range by altering the molar ratio of D-A. Figure 3b shows a comparison chart of the fluorescence intensity of the polymer. The fluorescence emission peak intensity shows a trend of decreasing first and then increasing, indicating that the probability of photogenerated electron and hole recombination decreases first and then increases. Spso-6, the polymer with the highest ratio of spirodifluorene and dibenzothioephene sulfone units, has the strongest fluorescence emission intensity, indicating that the structure of polymer Spso-6 may limit the migration of photogenerated electrons and holes under light irradiation so that the photogenerated electrons and holes can quickly recombine. Polymers Spso-2, Spso-3, and Spso-4 all have relatively low fluorescence emission intensities, indicating that the photogenerated electrons and holes generated by these three polymers can be better separated and migrated, which is helpful for the improvement of photocatalytic hydrogen production performance.

The fluorescence lifetime data of the six polymers are listed in Table 2, and the average fluorescence lifetime is calculated as follows [54]:

$$\tau_{\text{AVG}} = A1 \times \tau1 + A2 \times \tau2 + A3 \times \tau3 \quad (3)$$

As shown in Figure S1, the fluorescence lifetimes of the polymers are shorter, and all of them are in the nanosecond scale, at 2.95 ns, 2.42 ns, 2.45 ns, 0.93 ns, 1.85 ns, and 1.33 ns, respectively. Among all the polymers, the shorter lifetimes of the polymers with higher proportions of spirobifluorene, Spso-4~Spso-6, indicate that the probability of

photogenerated electrons and holes complexing in these polymers is higher, and they will be deactivated very quickly, which is unfavorable for the transport of the electrons to the surface of the materials and will affect the photocatalytic hydrogen-producing half-reaction. When the ratio of spirobifluorene to dibenzothiophene sulfone unit is less than 1:8, the polymer has a relatively long lifetime. This indicates that the D-A molar ratio in the polymer main chain has a substantial impact on the fluorescence lifetime of the polymers. When the D-A molar ratio is relatively low, the fluorescence lifetime of the material is relatively long. Conversely, when the molar ratio of D-A is relatively high, the fluorescence lifetime is relatively short. Longer fluorescence lifetimes would result in sufficient time for photogenerated electron/hole transfer, which in turn affects the performance of photocatalytic hydrogen production [55]. The D-A ratio affects the fluorescence lifetime of polymers as well. Transient photocurrent response testing provides further insight into the ability of polymers to transport photoinduced charge carriers. This measurement was carried out in four on/off cycles. The illumination used had wavelengths greater than 420 nm and an intensity of $100 \text{ mW} \cdot \text{cm}^{-2}$. As shown in Figure 3c, first, the *i-t* curves of all polymers had a good correlation with the process of switching the light on and off, indicating that the polymers all had good photocatalytic activity. Secondly, there were significant differences in the photocurrent intensity, and the photocurrent density from high to low was Sps0-3, Sps0-2, Sps0-4, Sps0-5, Sps0-1, and Sps0-6. Electrochemical impedance spectroscopy (EIS) characterizes the charge transport properties (Figure 3d), and Sps0-3 has the smallest Nyquist circle radius, suggesting that interfacial charge transfer is more efficient, which is consistent with the photocurrent response. These results combined with fluorescence emission spectroscopy and fluorescence lifetime results indicate that polymer Sps0-3 has better carrier separation efficiency.

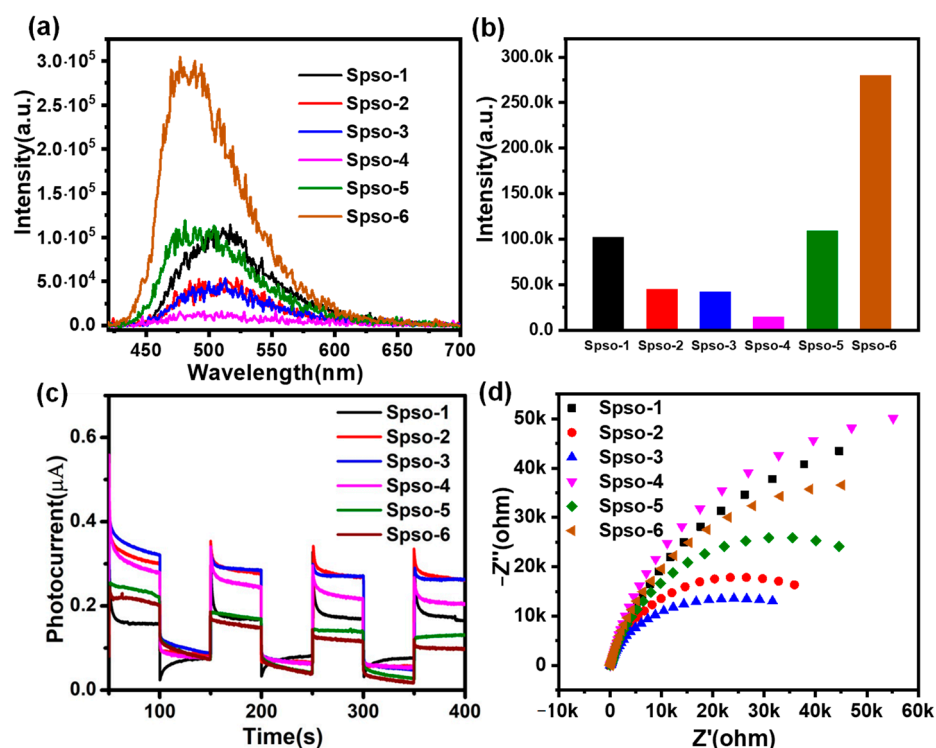


Figure 3. (a) Fluorescence emission spectra and (b) comparison diagram of fluorescence emission intensity of polymers. (c) Comparison of photocurrent behaviors of the polymers under visible light ($\lambda > 420 \text{ nm}$, $100 \text{ mW} \cdot \text{cm}^{-2}$). (d) Electrochemical impedance spectrum of the polymers.

Table 2. Fluorescence lifetime data of polymers.

Sample	τ_1 [ns] (Rel.%)	τ_2 [ns] (Rel.%)	τ_3 [ns] (Rel.%)	τ [ns]	χ^2
Sps0-1	1.12 (44.93)	3.34 (48.89)	13.30 (6.18)	2.95	1.155
Sps0-2	0.61 (33.38)	2.31 (54.79)	8.05 (11.83)	2.42	1.070
Sps0-3	0.91 (53.22)	2.88 (39.30)	11.24 (7.39)	2.45	1.139
Sps0-4	0.39 (79.74)	1.71 (16.66)	9.18 (3.61)	0.93	1.140
Sps0-5	0.59 (61.36)	2.18 (30.68)	10.32 (7.96)	1.85	1.287
Sps0-6	0.75 (55.59)	1.88 (42.73)	6.62 (1.68)	1.33	1.130

2.3. Photocatalytic Performance

The photocatalytic activity for hydrogen production was estimated for all the samples under visible light irradiation with wavelengths greater than 420 nm. The curves of H₂ evolution vs. irradiation time are shown in Figure 4a, with average hydrogen evolution rates (HERs) of 12, 21.2, 22.4, 18.6, 14.4, and 7.5 mmol g⁻¹ h⁻¹ for Sps0-1 to Sps0-6, respectively (Figure 4b). The HER initially increases and then decreases as the pyrene content increases. When Sps0-3 is used as a photocatalyst, the maximum HER of 22.4 mmol g⁻¹ h⁻¹ is obtained. Under visible light irradiation, this value is markedly higher than numerous other reported values of materials containing thiophene units [56–65]. These results indicate that the D-A ratio is a crucial variable in balancing photogenerated electron and hole segregation and transportation, which has an important impact on optimizing the photocatalytic performance of polymers [66]. These remarkable HER values imply that constructing D-A type CMPs could be an effective tactic for enhancing the photocatalytic water-splitting ability. The D-A structure can promote the separation of photogenerated electron/hole pairs, and the porous structure built on steric units offers sufficient space for the catalytic reaction. To study the relationship between light absorption and hydrogen production activity, polymer Sps0-3 was selected for the apparent quantum yield (AQY) test. AQY represents the ratio of the number of photons effectively utilized in the photochemical reaction to the total number of photons absorbed [67,68]. Monochromatic light filters with wavelengths of 420 nm, 450 nm, and 500 nm were used to conduct the photocatalytic experiment on polymer Sps0-3 for 3 h, under the reaction conditions of 40 mL of deionized water, 10 mL of triethanolamine, and 10 mg of the photocatalyst. The hydrogen production amounts of polymer Sps0-3 at 420 nm, 450 nm, and 500 nm for 1 h were 179, 140, and 30.3 mol g⁻¹ h⁻¹, respectively. The AQY values of polymer Sps0-3 at 420 nm, 450 nm, and 500 nm were 35.6%, 12.7%, and 1.82%, respectively. The AQY of polymer Sps0-3 at 420 nm was the highest, indicating that it had the highest utilization rate of 420 nm monochromatic light. This value is remarkably higher than the previously reported AQY value for comparable organic photocatalysts [57,58,62–65,69–71]. Consistent with the absorption spectrum, the HER of Sps0-3 decreased significantly at 500 nm, suggesting that the main hydrogen-producing photons are below 500 nm.

To prevent the palladium catalyst residue from causing photocatalytic testing errors, the palladium residue was determined by inductively coupled plasma mass spectrometry (ICP-MS). There was no obvious correlation between the hydrogen production activity of the polymer and the content of the palladium catalyst ($R^2 = 0.24$, Figure 4d). The lower residual concentration (0.23–0.68 wt%) is much lower than the addition of palladium in other organic photocatalytic systems as an adjunct (ca. 3 wt%). So while Pd residues were detected in the polymers, the low concentrations did not influence the regularity of the photocatalytic test results.

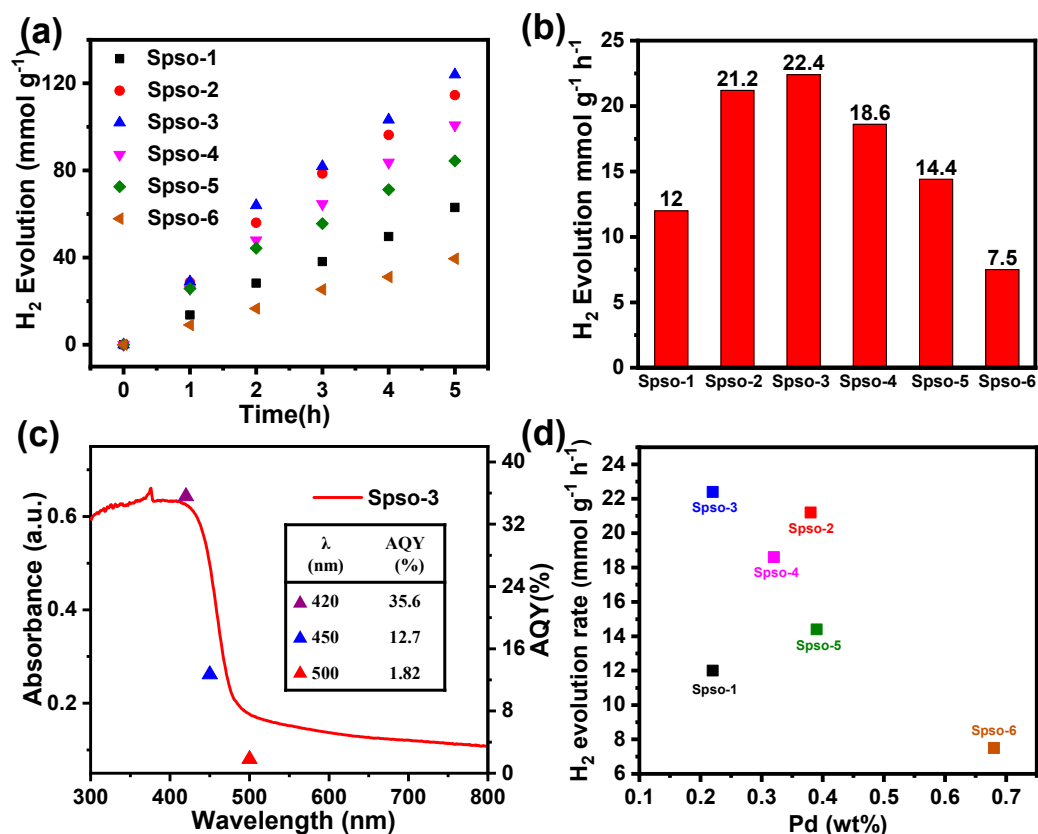


Figure 4. (a) Time-dependent hydrogen evolution with polymers lacking a metal cocatalyst under visible light illumination (wavelength > 420 nm, dosage of each photocatalyst is 10 mg). (b) Comparison of visible-light-driven H₂ production activity among the polymers (wavelength > 420 nm). (c) UV-vis diffuse reflectance spectrum and apparent quantum yields (at 420, 450, and 500 nm) of Sps0-3. (d) Correlation between photocatalytic hydrogen production activity and palladium residue.

The stability of this organic photocatalyst was evaluated by repeating experiments on Sps0-3. It was subjected to five consecutive photocatalytic cycles of 15 h (with each cycle being 5 h) under visible light irradiation. Using triethanolamine as the sacrificial agent, every 5 h was taken as a hydrogen production cycle, and the sacrificial agent was replenished and degassed. As shown in Figure 5a, we observed that after 15 h of continuous visible light catalytic testing, the rate of hydrogen production by polymer Sps0-3 hardly decreased, indicating that there was no harmful photochemical degradation of Sps0-3 during illumination, and it was a stable photocatalyst. Following a 15 h photocatalytic reaction, the recovered Sps0-3 was analyzed using UV-vis adsorption spectra (Figure 5b), PXRD (Figure 5c), and FT-IR (Figure 5d). Sps0-3 retains its original structure and crystallinity well after the photocatalytic reaction, resulting in excellent photocatalytic cycling stability. Moreover, by comparing the peak PXRD intensity before and after photocatalysis, a certain degree of decrease in the crystallinity of Sps0-3 is observed. After a 15 h photocatalytic reaction under visible light ($\lambda > 420$ nm), the flake morphology of Sps0-3 became smooth, which may have caused a partial decrease in the photocatalytic performance (Figure 5e,f). The above results indicate that Sps0-3 possesses outstanding HER performance and remarkable long-time stability, possessing the potential to be a good polymer photocatalytic material.

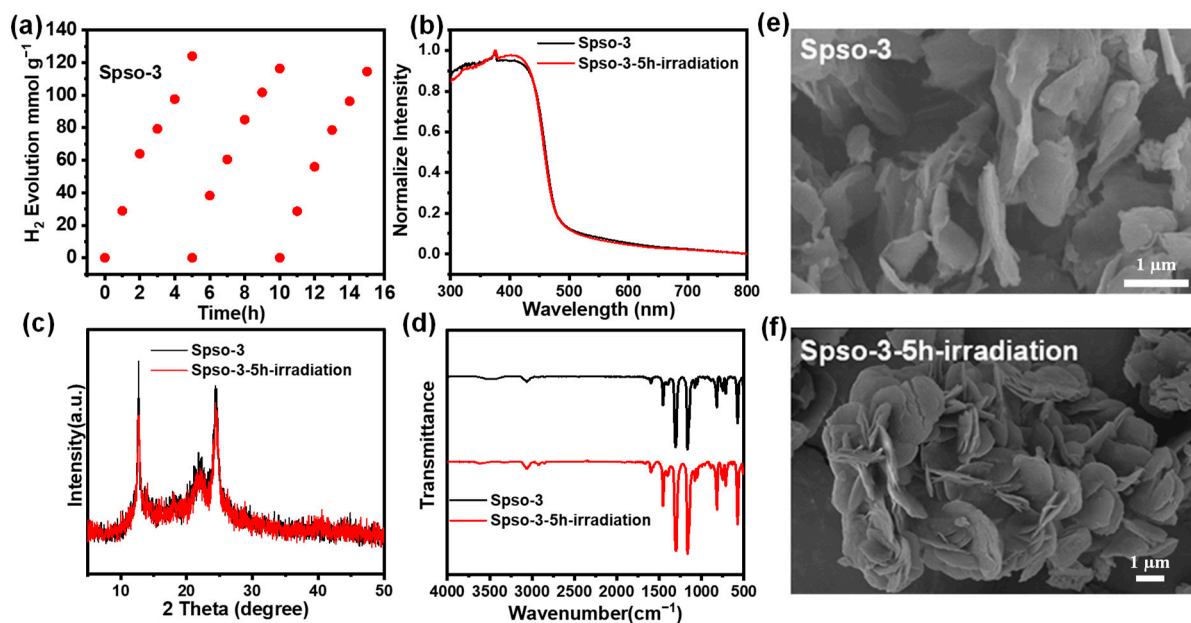


Figure 5. (a) Stability test using Spsso-3 in water over a time period of 25 h ($\lambda > 420$ nm). (b) UV-vis adsorption spectra, (c) PXRD spectra, (d) FT-IR spectra, and (e,f) SEM images of Spsso-3 before and after the photocatalytic cycling experiments.

3. Materials and Methods

3.1. Materials and Reagents

In this study, Dibenzothiophene sulfone (purity 99.28%), Pinacol bis(boronic acid) ester (purity 98%), 1,1'-bis (diphenylphosphine) ferrocene] palladium dichloride (purity 98%), Tetri (triphenylphosphine) palladium (purity 98%), 1,3,6,8-tetrabromopyrene (purity of 98%), 2,2',7,7'-tetrabromo-9,9'-spirodifluorene (M1, purity greater than 97%), 1,4-dioxane (AR), anhydrous potassium carbonate (AR), potassium acetate (AR), anhydrous magnesium sulfate (AR), barium sulfate (AR), sodium bicarbonate (AR), sulfuric acid (purity 98%), nitric acid (AR), hydrochloric acid (AR), N,N-Dimethylformamide (AR), methanol (AR), dichloromethane (AR), ethanol (AR), acetone (AR) and tetrahydrofuran (THF, AR) were used. All reactions and manipulations were carried out under an argon atmosphere by using standard Schlenk techniques or an inter-atmosphere glovebox. Before use, all the solvents were dried by refluxing with sodium and benzophenone and degassed by applying three freeze-pump-thaw cycles. Chloroform-d was dried by using a 4 Å molecular sieve (2–3 days). All chemicals (reagents and solvents) were obtained from commercial suppliers (Energy Chemical, Heowns, Tianjin, China) and directly used without further purification.

3.2. Polymer Synthesis Methods

3.2.1. Synthesis of 3,7-Dibromo-dibenzothiophene Sulfone (M2)

Dibenzothiophene sulfone monomer (7.0 g, 32.4 mmol) was dissolved in 240 mL concentrated sulfuric acid in an atmosphere of argon, and n-bromosuccinimide (NBS) (12 g, 67.4 mmol) was added slowly in three batches. The mixture was then stirred at room temperature for 24 h. After the reaction was complete, the reaction solution was slowly poured into a large amount of ice water for dilution. The solids were filtered and then washed with water and a solution of saturated sodium bicarbonate until the pH was neutral. After drying in a vacuum drying oven, the pure white solid was obtained by repeated recrystallization with trichloromethane (150 mL \times 3) three times (5.5 g, 45%). ¹H NMR (400 MHz, CDCl₃): δ 7.93 (s, 2H), 7.76–7.78 (d, J = 8.0 Hz, 2H), 7.62–7.64 (d, J = 8.0 Hz, 2H).

3.2.2. Synthesis of 3,7-Diborate Ester-dibenzothiophene Sulfone (M3)

3,7-Dibromo-dibenzothiophene sulfone (4.1 g, 10.7 mmol), pinacol borate (8.4 g, 33.0 mmol), and potassium acetate (6.3 g, 6.3 mmol) were mixed in a 250 mL round-bottom flask under the protection of argon. [1,1'-bis(diphenylphosphonyl)ferrocene] palladium dichloride (0.40 g, 0.5 mmol) was dissolved in 120 mL dried 1,4-dioxane, and reacted at 106 °C for 24 h. After the reaction, about 150 mL water was added to the reaction mixture, and then 100 mL dichloromethane was extracted 3 times. The organic phase was combined and dried with anhydrous magnesium sulfate, and the organic solvent was removed by rotary evaporation. The solid crude product was purified by a silica gel column (petroleum ether: dichloromethane = 2:1), and the white solid M3 was obtained (2.6 g, 50%). ¹H NMR (400 MHz, CDCl₃): δ 8.27 (s, 2H), 8.04–8.06 (d, *J* = 8.0 Hz, 2H), 7.79–7.81 (d, *J* = 8.0 Hz, 2H), 1.36 (s, 24H).

3.2.3. Typical Procedure of Suzuki–Miyaura Coupling Polymerization

Shown as Scheme 1, under anaerobic and anhydrous conditions, 2,2',7,7'-tetrabromo-9,9'-spirodifluorene (M1), 3,7-dibromo-dibenzothiophene sulfone (M2), 3,7-diborate ester dibenzothiophene sulfone (M3), Pd(PPh₃)₄ (5%) and K₂CO₃ were dissolved in mixed solvent of degassed DMF and degassed H₂O. Then, the reaction was refluxed at 130 °C for 48 h. After cooling to room temperature, the reaction mixture was filtered through the funnel to gain crude product, the polymer was further purified and washed with H₂O, MeOH, CH₂Cl₂, THF, and acetone. Then, the resulting polymers were subjected to Soxhlet extraction using THF for 48 h to remove the undesirable impurities.

3.2.4. Synthesis of Spso-1

M2 (0.187 g, 0.50 mmol), M3 (0.234 g, 0.50 mmol), anhydrous potassium carbonate (0.830 g, 6.0 mmol), tetraphenylphosphine palladium (0.0125 g, 8.7 μmol), 16 mL of *N,N*-dimethylformamide, and 3 mL of water were used for Suzuki–Miyaura coupling polymerization. The yellow-green solid was obtained, the yield was 0.213 g, and the yield was 82% (Pd: 0.22 wt%).

3.2.5. Synthesis of Spso-2

M1 (0.0152 g, 0.024 mmol), M2 (0.169 g, 0.45 mmol), M3 (0.234 g, 0.50 mmol), anhydrous potassium carbonate (0.830 g, 6.0 mmol), tetraphenylphosphine palladium (0.0125 g, 8.7 μmol), 16 mL of *N,N*-dimethylformamide, and 3 mL of water were used for Suzuki–Miyaura coupling polymerization. The yellow-green solid was obtained, the yield was 0.163 g, and the yield was 78% (Pd: 0.38 wt%).

3.2.6. Synthesis of Spso-3

M1 (0.0284 g, 0.045 mmol), M2 (0.153 g, 0.41 mmol), M3 (0.234 g, 0.50 mmol), anhydrous potassium carbonate (0.830 g, 6.0 mmol), tetraphenylphosphine palladium (0.0125 g, 8.7 μmol), 16 mL of *N,N*-dimethylformamide, and 3 mL of water were used for Suzuki–Miyaura coupling polymerization. The yellow-green solid was obtained, the yield was 0.162 g, and the yield was 77% (Pd: 0.22 wt%).

3.2.7. Synthesis of Spso-4

M1 (0.0632 g, 0.10 mmol), M2 (0.112 g, 0.30 mmol), M3 (0.234 g, 0.50 mmol), anhydrous potassium carbonate (0.830 g, 6.0 mmol), tetraphenylphosphine palladium (0.0125 g, 8.7 μmol), 16 mL of *N,N*-dimethylformamide, and 3 mL of water were used for Suzuki–Miyaura coupling polymerization. The yellow-green solid was obtained, the yield was 0.202 g, and the yield was 98% (Pd: 0.32 wt%).

3.2.8. Synthesis of Spso-5

M1 (0.105 g, 0.17 mmol), M2 (0.0625 g, 0.17 mmol), M3 (0.234 g, 0.50 mmol), anhydrous potassium carbonate (0.830 g, 6.0 mmol), tetraphenylphosphine palladium

(0.0125 g, 8.7 μmol), 16 mL of N,N-dimethylformamide, and 3 mL of water were used for Suzuki–Miyaura coupling polymerization. The green solid was obtained, the yield was 0.171 g, and the yield was 83% (Pd: 0.39 wt%).

3.2.9. Synthesis of Spso-6

M1 (0.158 g, 0.25 mmol), M3 (0.234 g, 0.50 mmol), anhydrous potassium carbonate (0.830 g, 6.0 mmol), tetraphenylphosphine palladium (0.0125 g, 8.7 μmol), 16 mL of N,N-dimethylformamide, and 3 mL of water were used for Suzuki–Miyaura coupling polymerization. The green solid was obtained, the yield was 0.183 g, and the yield was 99% (Pd: 0.68 wt%).

3.3. Instrumentation/General Methods

The Fourier transform infrared (FTIR) spectra of the samples were recorded with a Bruker Vertex 70 (Billerica, MA, USA) at room temperature by using the conventional KBr pellet method. Thermogravimetric analysis was performed on a NETZSCH STA449C (Netzsch GmbH, Selb, Germany) instrument under nitrogen flow at a heating rate of $10\text{ }^{\circ}\text{C min}^{-1}$ up to $800\text{ }^{\circ}\text{C}$. The surface morphology of the polymers was evaluated with a Hitachi S4800 Cold Field Emission SEM (Tokyo, Japan). The Powder X-ray diffraction (PXRD) measurements were performed using X-ray diffraction (X'pert pro, PANalytical, Almelo, The Netherlands), equipped with Cu K α radiation ($\lambda = 1.54056\text{ \AA}$) at the scattering angle 2θ between 3 and 50° . The UV–visible absorption spectra of the polymers were recorded for the dry-pressed disk samples on a Carry 5000 UV–Vis–NIR spectrometer (Agilent, Santa Clara, CA, USA). The fluorescence data were measured on an FLS920 fluorescence spectrophotometer (Edinburgh Instruments, Livingston, UK) with the polymer powders and optically dilute solutions ($A < 0.1$). Time-correlated single-photon counting experiments were performed on an Edinburgh FLS920 fluorescence spectrophotometer with picosecond pulsed LED excitation sources and an R928 detector (Agilent, Santa Clara, CA, USA). An EPLED-330 diode ($\lambda = 334.6\text{ nm}$, instrument response 881.6 ps, bandwidth 9.6 nm, Edinburgh Instruments, UK) was used as the light source. Decay times were fitted in the F900 software (ver. 7.1.3) using suggested lifetime estimates. Photocurrent response was recorded using a CHI-660E electrochemical workstation (CH Instruments, Shanghai, China) in a standard three-electrode configuration. The polymers (2.0 mg) were dispersed in ethanol (0.5 mL) containing 1% Nafion by ultrasound for 1 h. The work electrodes were prepared via drop-casting the mixture of 200 μL onto the surface of the FTO glass substrate electrode and then filmed at $80\text{ }^{\circ}\text{C}$ in a vacuum oven. The Pt plate served as the counter electrode, and a saturated Ag/AgCl electrode as a reference electrode. A 0.5 M Na_2SO_4 solution was used as the electrolyte. Sunlight was simulated with a 300 W Xenon lamp (Hefan Instrument, Shanghai, China) and a 420 nm cut-off filter.

3.4. Photocatalytic Activity Measurements

A flask was charged with the polymer powder (10.0 mg), a 4:1 vol. mixture of water and triethanolamine. The resulting suspension was ultrasonicated until the photocatalyst was dispersed before degassing by N_2 bubbling for 30 min. The accumulated number of evolved gases was monitored every 60 min using a gas chromatograph (450-GC, Varian, Palo Alto, CA, USA) equipped with a thermal conductive detector (TCD). The light source was a 300 W Xe lamp with a cut-off filter applied to generate visible light ($\lambda > 420\text{ nm}$). Hydrogen was detected with a TCD detector, referencing standard gases with known concentrations of hydrogen. Hydrogen dissolved in the reaction mixture was not measured, and the pressure increase generated by the evolved hydrogen was neglected in the calculations.

3.5. AQY Measurements

The apparent quantum yield (AQY) for H_2 evolution was measured using monochromatic visible light at 420 nm. The energy (E) of irradiation was determined to be 30 mW cm^{-1}

by a calibrated power meter. The irradiation area was controlled at 9.8 cm². Depending on the amount of hydrogen produced by the photocatalytic reaction in an average of 3 h, the AQY was calculated with the following equation:

$$\text{AQY} = \frac{N_e}{N_p} \times 100\% \quad (4)$$

$$= \frac{2 \times M \times N_A \times h \times c}{S \times P \times t \times \lambda} \times 100\% \quad (5)$$

where M is the amount of H₂ (mol), N_A is the Avogadro constant (6.022×10^{23} /mol), h is the Planck constant (6.626×10^{-34} J·s), c is the speed of light (3×10^8 m/s), S is the irradiation area (cm²), P is the intensity of irradiation light (W/cm²), t is the photoreaction time (s), λ is the wavelength of the monochromatic light (m).

4. Conclusions

In conclusion, the D-A type CMP photocatalysts with spirobifluorene as the core unit and dibenzothiophene sulfone as the electron acceptor were successfully synthesized. Crosslinked pore structures were successfully constructed and the specific surface area increased with the ratio of spirobifluorene. When the molar ratio of D-A was 1:20, the polymer Spso-3 showed the highest photocatalytic hydrogen production activity of 22.4 mmol h⁻¹ g⁻¹, which was probably caused by the increase in the photo-induced carrier separation efficiency, indicating that the photocatalytic performance depended on the molar ratio of D-A in the skeleton. These results indicate that the D-A ratio is a crucial variable in balancing photogenerated electron and hole segregation and transportation, which has an important impact on optimizing the photocatalytic performance of polymers. The D-A structure can promote the separation of photogenerated electron/hole pairs, and the porous structure built on steric units offers sufficient space for the catalytic reaction. All the findings suggest that the construction of D-A type CMPs could be an efficient approach to improve the photocatalytic performance for water splitting.

Supplementary Materials: The following supporting information can be downloaded at: <https://www.mdpi.com/article/10.3390/catal14100717/s1>, Figure S1: The average fluorescence lifetimes of polymers.

Author Contributions: Conceptualization, H.Z. and X.P.; methodology, P.S., H.X., L.L., J.W. and X.X.; validation, X.X. and P.S.; formal analysis, S.S. and W.L.; investigation, Z.K.; resources, X.P.; data curation, H.Z.; writing—original draft preparation, H.Z.; writing—review and editing, X.P.; supervision, X.P.; project administration, H.Z. All authors have read and agreed to the published version of the manuscript.

Funding: This research was funded by Shandong Provincial Natural Science Foundation, grant number ZR2023QE014; and National Natural Science Foundation of China, grant number 22171111.

Data Availability Statement: Dataset available on request from the authors.

Acknowledgments: The authors thank the Supercomputing Center of Lanzhou University for the DFT calculations.

Conflicts of Interest: The authors declare no conflicts of interest.

References

1. Lubitz, W.; Tumas, W. Hydrogen: An Overview. *Chem. Rev.* **2007**, *107*, 3900–3903. [[CrossRef](#)] [[PubMed](#)]
2. Chen, X.; Shen, S.; Guo, L.; Mao, S.S. Semiconductor-based Photocatalytic Hydrogen Generation. *Chem. Rev.* **2010**, *110*, 6503–6570. [[CrossRef](#)] [[PubMed](#)]
3. Dawood, F.; Anda, M.; Shafiullah, G.M. Hydrogen production for energy: An overview. *Int. J. Hydrogen Energy* **2020**, *45*, 3847–3869. [[CrossRef](#)]
4. Colón, G. Towards the hydrogen production by photocatalysis. *Appl. Catal. A-Gen.* **2016**, *518*, 48–59. [[CrossRef](#)]
5. Wang, Q.; Domen, K. Particulate Photocatalysts for Light-Driven Water Splitting: Mechanisms, Challenges, and Design Strategies. *Chem. Rev.* **2020**, *120*, 919–985. [[CrossRef](#)]

6. Hisatomi, T.; Domen, K. Overall water splitting: What's next? *Next Energy* **2023**, *1*, 100006. [[CrossRef](#)]
7. Kudo, A.; Miseki, Y. Heterogeneous photocatalyst materials for water splitting. *Chem. Soc. Rev.* **2009**, *38*, 253–278. [[CrossRef](#)]
8. Wang, X.; Maeda, K.; Thomas, A.; Takanabe, K.; Xin, G.; Carlsson, J.M.; Domen, K.; Antonietti, M. A metal-free polymeric photocatalyst for hydrogen production from water under visible light. *Nat. Mater.* **2009**, *8*, 76–80. [[CrossRef](#)]
9. Ong, W.-J.; Tan, L.-L.; Ng, Y.H.; Yong, S.-T.; Chai, S.-P. Graphitic Carbon Nitride (g-C₃N₄)-Based Photocatalysts for Artificial Photosynthesis and Environmental Remediation: Are We a Step Closer to Achieving Sustainability? *Chem. Rev.* **2016**, *116*, 7159–7329. [[CrossRef](#)]
10. Fateminia, S.M.A.; Mao, Z.; Xu, S.; Yang, Z.; Chi, Z.; Liu, B. Organic Nanocrystals with Bright Red Persistent Room-Temperature Phosphorescence for Biological Applications. *Angew. Chem. Int. Ed.* **2017**, *56*, 12160–12164. [[CrossRef](#)]
11. Cai, S.; Shi, H.; Zhang, Z.; Wang, X.; Ma, H.; Gan, N.; Wu, Q.; Cheng, Z.; Ling, K.; Gu, M.; et al. Hydrogen-Bonded Organic Aromatic Frameworks for Ultralong Phosphorescence by Intralayer π - π Interactions. *Angew. Chem. Int. Ed.* **2018**, *57*, 4005–4009. [[CrossRef](#)] [[PubMed](#)]
12. Sprick, R.S.; Bonillo, B.; Clowes, R.; Guiglion, P.; Brownbill, N.J.; Slater, B.J.; Blanc, F.; Zwiijnenburg, M.A.; Adams, D.J.; Cooper, A.I. Visible-Light-Driven Hydrogen Evolution Using Planarized Conjugated Polymer Photocatalysts. *Angew. Chem. Int. Ed.* **2016**, *55*, 1792–1796. [[CrossRef](#)] [[PubMed](#)]
13. Zhang, G.; Lan, Z.-A.; Wang, X. Conjugated Polymers: Catalysts for Photocatalytic Hydrogen Evolution. *Angew. Chem. Int. Ed.* **2016**, *55*, 15712–15727. [[CrossRef](#)] [[PubMed](#)]
14. Bai, Y.; Wilbraham, L.; Slater, B.J.; Zwiijnenburg, M.A.; Sprick, R.S.; Cooper, A.I. Accelerated Discovery of Organic Polymer Photocatalysts for Hydrogen Evolution from Water through the Integration of Experiment and Theory. *J. Am. Chem. Soc.* **2019**, *141*, 9063–9071. [[CrossRef](#)] [[PubMed](#)]
15. Zhao, C.; Chen, Z.; Shi, R.; Yang, X.; Zhang, T. Recent Advances in Conjugated Polymers for Visible-Light-Driven Water Splitting. *Adv. Mater.* **2020**, *32*, 1907296. [[CrossRef](#)] [[PubMed](#)]
16. Yin, X.; Guo, F.; Lalancette, R.A.; Jäkle, F. Luminescent Main-Chain Organoborane Polymers: Highly Robust, Electron-Deficient Poly(oligothiophene borane)s via Stille Coupling Polymerization. *Macromolecules* **2016**, *49*, 537–546. [[CrossRef](#)]
17. Li, L.; Hadt, R.G.; Yao, S.; Lo, W.-Y.; Cai, Z.; Wu, Q.; Pandit, B.; Chen, L.X.; Yu, L. Photocatalysts Based on Cobalt-Chelating Conjugated Polymers for Hydrogen Evolution from Water. *Chem. Mater.* **2016**, *28*, 5394–5399. [[CrossRef](#)]
18. Lan, Z.-A.; Ren, W.; Chen, X.; Zhang, Y.; Wang, X. Conjugated donor-acceptor polymer photocatalysts with electron-output “tentacles” for efficient hydrogen evolution. *Appl. Catal. B Environ.* **2019**, *245*, 596–603. [[CrossRef](#)]
19. Lee, J.-S.M.; Cooper, A.I. Advances in Conjugated Microporous Polymers. *Chem. Rev.* **2020**, *120*, 2171–2214. [[CrossRef](#)]
20. Han, C.; Dong, P.; Tang, H.; Zheng, P.; Zhang, C.; Wang, F.; Huang, F.; Jiang, J.-X. Realizing high hydrogen evolution activity under visible light using narrow band gap organic photocatalysts. *Chem. Sci.* **2021**, *12*, 1796–1802. [[CrossRef](#)]
21. Xu, F.; Yang, S.; Chen, X.; Liu, Q.; Li, H.; Wang, H.; Wei, B.; Jiang, D. Energy-storage covalent organic frameworks: Improving performance via engineering polysulfide chains on walls. *Chem. Sci.* **2019**, *10*, 6001–6006. [[CrossRef](#)] [[PubMed](#)]
22. Pachfule, P.; Acharjya, A.; Roeser, J.; Langenhahn, T.; Schwarze, M.; Schomacker, R.; Thomas, A.; Schmidt, J. Diacetylene Functionalized Covalent Organic Framework (COF) for Photocatalytic Hydrogen Generation. *J. Am. Chem. Soc.* **2018**, *140*, 1423–1427. [[CrossRef](#)] [[PubMed](#)]
23. Wang, X.; Chen, L.; Chong, S.Y.; Little, M.A.; Wu, Y.; Zhu, W.-H.; Clowes, R.; Yan, Y.; Zwiijnenburg, M.A.; Sprick, R.S.; et al. Sulfone-containing covalent organic frameworks for photocatalytic hydrogen evolution from water. *Nat. Chem.* **2018**, *10*, 1180–1189. [[CrossRef](#)] [[PubMed](#)]
24. Kochergin, Y.S.; Schwarz, D.; Acharjya, A.; Ichangi, A.; Kulkarni, R.; Eliášová, P.; Vacek, J.; Schmidt, J.; Thomas, A.; Bojdys, M.J. Exploring the “Goldilocks Zone” of Semiconducting Polymer Photocatalysts by Donor–Acceptor Interactions. *Angew. Chem. Int. Ed.* **2018**, *57*, 14188–14192. [[CrossRef](#)] [[PubMed](#)]
25. Lan, Z.-A.; Zhang, G.; Chen, X.; Zhang, Y.; Zhang, K.A.I.; Wang, X. Reducing the Exciton Binding Energy of Donor–Acceptor-Based Conjugated Polymers to Promote Charge-Induced Reactions. *Angew. Chem. Int. Ed.* **2019**, *58*, 10236–10240. [[CrossRef](#)]
26. Huang, W.; He, Q.; Hu, Y.; Li, Y. Molecular Heterostructures of Covalent Triazine Frameworks for Enhanced Photocatalytic Hydrogen Production. *Angew. Chem. Int. Ed.* **2019**, *58*, 8676–8680. [[CrossRef](#)]
27. Fukuzumi, S.; Ohkubo, K. Selective photocatalytic reactions with organic photocatalysts. *Chem. Sci.* **2013**, *4*, 561–574. [[CrossRef](#)]
28. Ru, C.; Chen, P.; Wu, X.; Chen, C.; Zhang, J.; Zhao, H.; Wu, J.; Pan, X. Enhanced Built-in Electric Field Promotes Photocatalytic Hydrogen Performance of Polymers Derived from the Introduction of B \leftarrow N Coordination Bond. *Adv. Sci.* **2022**, *9*, 2204055. [[CrossRef](#)]
29. Wu, X.; Zhang, M.; Xia, Y.; Ru, C.; Chen, P.; Zhao, H.; Zhou, L.; Gong, C.; Wu, J.; Pan, X. Arylboron functional covalent organic frameworks for synergistic photocatalytic hydrogen evolution. *J. Mater. Chem. A* **2022**, *10*, 17691–17698. [[CrossRef](#)]
30. Zhao, H.; Dong, Y.; Sun, P.; Bai, Y.; Ru, C.; Wu, X.; Li, Z.; Han, X.; Wu, J.; Pan, X. Effect of D/A Ratio on Photocatalytic Hydrogen Evolution Performance of Conjugated Polymer Photocatalysts. *ACS Appl. Energy Mater.* **2022**, *5*, 4631–4640. [[CrossRef](#)]
31. Chen, P.; Ru, C.; Hu, L.; Yang, X.; Wu, X.; Zhang, M.; Zhao, H.; Wu, J.; Pan, X. Construction of Efficient D–A-Type Photocatalysts by B–N Bond Substitution for Water Splitting. *Macromolecules* **2023**, *56*, 858–866. [[CrossRef](#)]
32. Fournier, J.-H.; Maris, T.; Wuest, J.D. Molecular Tectonics. Porous Hydrogen-Bonded Networks Built from Derivatives of 9,9'-Spirobifluorene. *J. Org. Chem.* **2004**, *69*, 1762–1775. [[CrossRef](#)] [[PubMed](#)]

33. Heredia, D.; Natera, J.; Gervaldo, M.; Otero, L.; Fungo, F.; Lin, C.-Y.; Wong, K.-T. Spirobifluorene-Bridged Donor/Acceptor Dye for Organic Dye-Sensitized Solar Cells. *Org. Lett.* **2010**, *12*, 12–15. [[CrossRef](#)] [[PubMed](#)]
34. Qiu, N.; Yang, X.; Zhang, H.; Wan, X.; Li, C.; Liu, F.; Zhang, H.; Russell, T.P.; Chen, Y. Nonfullerene Small Molecular Acceptors with a Three-Dimensional (3D) Structure for Organic Solar Cells. *Chem. Mater.* **2016**, *28*, 6770–6778. [[CrossRef](#)]
35. Lyu, Y.-Y.; Kwak, J.; Jeon, W.S.; Byun, Y.; Lee, H.S.; Kim, D.; Lee, C.; Char, K. Highly Efficient Red Phosphorescent OLEDs based on Non-Conjugated Silicon-Cored Spirobifluorene Derivative Doped with Ir-Complexes. *Adv. Funct. Mater.* **2009**, *19*, 420–427. [[CrossRef](#)]
36. Wu, C.; Liu, Y.; Liu, H.; Duan, C.; Pan, Q.; Zhu, J.; Hu, F.; Ma, X.; Jiu, T.; Li, Z.; et al. Highly Conjugated Three-Dimensional Covalent Organic Frameworks Based on Spirobifluorene for Perovskite Solar Cell Enhancement. *J. Am. Chem. Soc.* **2018**, *140*, 10016–10024. [[CrossRef](#)]
37. Han, C.; Xiang, S.; Jin, S.; Luo, L.-W.; Zhang, C.; Yan, C.; Jiang, J.-X. Linear multiple-thiophene-containing conjugated polymer photocatalysts with narrow band gaps for achieving ultrahigh photocatalytic hydrogen evolution activity under visible light. *J. Mater. Chem. A* **2022**, *10*, 5255–5261. [[CrossRef](#)]
38. Kotp, M.G.; Torad, N.L.; Nara, H.; Chaikittisilp, W.; You, J.; Yamauchi, Y.; El-Mahdy, A.F.M.; Kuo, S.-W. Tunable thiophene-based conjugated microporous polymers for the disposal of toxic hexavalent chromium. *J. Mater. Chem. A* **2023**, *11*, 15022–15032. [[CrossRef](#)]
39. Li, Z.; Zhao, F.; Chu, Y.; Meng, F.; Dong, Y.; Zhang, H.; Zhao, J.; Du, Y.; Wang, S. Fused-Thiophene and Sulfone-Based Donor–Acceptor Conjugated Polymers for Enhanced Hydrogen Production. *ACS Sustain. Chem. Eng.* **2024**, *12*, 1072–1083. [[CrossRef](#)]
40. Yu, C.; Zhou, W.; Yu, J.; Cao, F.; Li, X. Thermal Stability, Microstructure and Photocatalytic Activity of the Bismuth Oxybromide Photocatalyst. *Chin. J. Chem.* **2012**, *30*, 721–726. [[CrossRef](#)]
41. Chen, H.-Y.; Yeh, S.-C.; Chen, C.-T.; Chen, C.-T. Comparison of thiophene- and selenophene-bridged donor–acceptor low band-gap copolymers used in bulk-heterojunction organic photovoltaics. *J. Mater. Chem.* **2012**, *22*, 21549–21559. [[CrossRef](#)]
42. He, Y.; Liu, Y.; Li, C.; Chen, X.-B.; Shi, Z.; Feng, S. Origin of the Photocatalytic Activity of Crystalline Phase Structures. *ACS Appl. Energy Mater.* **2022**, *5*, 8923–8929. [[CrossRef](#)]
43. Li, S.; Liu, W.; Shi, M.; Mai, J.; Lau, T.-K.; Wan, J.; Lu, X.; Li, C.-Z.; Chen, H. A spirobifluorene and diketopyrrolopyrrole moieties based non-fullerene acceptor for efficient and thermally stable polymer solar cells with high open-circuit voltage. *Energy Environ. Sci.* **2016**, *9*, 604–610. [[CrossRef](#)]
44. Otero, L.; Sereno, L.; Fungo, F.; Liao, Y.-L.; Lin, C.-Y.; Wong, K.-T. Synthesis and Properties of a Novel Electrochromic Polymer Obtained from the Electropolymerization of a 9,9'-Spirobifluorene-Bridged Donor–Acceptor (D–A) Bichromophore System. *Chem. Mater.* **2006**, *18*, 3495–3502. [[CrossRef](#)]
45. Modak, A.; Maegawa, Y.; Goto, Y.; Inagaki, S. Synthesis of 9,9'-spirobifluorene-based conjugated microporous polymers by FeCl₃-mediated polymerization. *Poly. Chem.* **2016**, *7*, 1290–1296. [[CrossRef](#)]
46. Wu, F.-I.; Dodda, R.; Reddy, D.S.; Shu, C.-F. Synthesis and characterization of spiro-linked poly(terfluorene): A blue-emitting polymer with controlled conjugated length. *J. Mater. Chem.* **2002**, *12*, 2893–2897. [[CrossRef](#)]
47. Das, S.; Chowdhury, I.H.; Chakraborty, A.; Naskar, M.K.; Sarkar, M.; Manirul Islam, S.K. Porous organic polymer (POP) nanosheets: An efficient photo-catalyst for visible-light assisted CO₂ reduction. *Mater. Adv.* **2022**, *3*, 3165–3173. [[CrossRef](#)]
48. Liu, R.; Yu, Z.; Zhang, R.; Xiong, J.; Qiao, Y.; Liu, X.; Lu, X. Hollow Nanoreactors for Controlled Photocatalytic Behaviors: Fundamental Theory, Structure–Performance Relationship, and Catalytic Advantages. *Small* **2024**, *20*, 2308142. [[CrossRef](#)]
49. Niu, P.; Zhang, L.; Liu, G.; Cheng, H.-M. Graphene-Like Carbon Nitride Nanosheets for Improved Photocatalytic Activities. *Adv. Funct. Mater.* **2012**, *22*, 4763–4770. [[CrossRef](#)]
50. Zhou, M.; Lou, X.W.; Xie, Y. Two-dimensional nanosheets for photoelectrochemical water splitting: Possibilities and opportunities. *Nano Today* **2013**, *8*, 598–618. [[CrossRef](#)]
51. Narsaria, A.K.; Poater, J.; Guerra, C.F.; Ehlers, A.W.; Hamlin, T.A.; Lammertsma, K.; Bickelhaupt, F.M. Distortion-Controlled Redshift of Organic Dye Molecules. *Chem. Eur. J.* **2020**, *26*, 2080–2093. [[CrossRef](#)] [[PubMed](#)]
52. Zhang, H.; Zhang, J.; Ye, R.; Xu, S.; Bai, G. Color modulation of cerium sulfide colorant powders through chemical doping engineering. *J. Mater. Chem. C* **2023**, *11*, 9215–9222. [[CrossRef](#)]
53. Ravishankar, S.; Bisquert, J.; Kirchartz, T. Interpretation of Mott–Schottky plots of photoanodes for water splitting. *Chem. Sci.* **2022**, *13*, 4828–4837. [[CrossRef](#)] [[PubMed](#)]
54. Berezin, M.Y.; Achilefu, S. Fluorescence Lifetime Measurements and Biological Imaging. *Chem. Rev.* **2010**, *110*, 2641–2684. [[CrossRef](#)] [[PubMed](#)]
55. Shang, Y.; Li, W.; Ma, Y.; Li, B.; Xu, Q.; Du, Y.; Peng, Y.; Wang, Y.; Zhu, Y. Rapid Hole Generation via D–A Structure-Dependent Built-In Electric Field of Deacetylated Chitin-PDI for Efficient Photocatalytic Oxidation. *Adv. Funct. Mater.* **2024**, 2406533. [[CrossRef](#)]
56. Wang, Z.; Yang, X.; Yang, T.; Zhao, Y.; Wang, F.; Chen, Y.; Zeng, J.H.; Yan, C.; Huang, F.; Jiang, J.-X. Dibenzothiophene Dioxide Based Conjugated Microporous Polymers for Visible-Light-Driven Hydrogen Production. *ACS Catal.* **2018**, *8*, 8590–8596. [[CrossRef](#)]
57. Zhao, Y.; Ma, W.; Xu, Y.; Zhang, C.; Wang, Q.; Yang, T.; Gao, X.; Wang, F.; Yan, C.; Jiang, J.-X. Effect of Linking Pattern of Dibenzothiophene-S,S-dioxide-Containing Conjugated Microporous Polymers on the Photocatalytic Performance. *Macromolecules* **2018**, *51*, 9502–9508. [[CrossRef](#)]

58. Sprick, R.S.; Bai, Y.; Guilbert, A.A.Y.; Zbiri, M.; Aitchison, C.M.; Wilbraham, L.; Yan, Y.; Woods, D.J.; Zwijnenburg, M.A.; Cooper, A.I. Photocatalytic Hydrogen Evolution from Water Using Fluorene and Dibenzothiophene Sulfone-Conjugated Microporous and Linear Polymers. *Chem. Mater.* **2019**, *31*, 305–313. [[CrossRef](#)]
59. Meier, C.B.; Clowes, R.; Berardo, E.; Jelfs, K.E.; Zwijnenburg, M.A.; Sprick, R.S.; Cooper, A.I. Structurally Diverse Covalent Triazine-Based Framework Materials for Photocatalytic Hydrogen Evolution from Water. *Chem. Mater.* **2019**, *31*, 8830–8838. [[CrossRef](#)]
60. Chen, W.; Wang, L.; Mo, D.; He, F.; Wen, Z.; Wu, X.; Xu, H.; Chen, L. Modulating Benzothiadiazole-Based Covalent Organic Frameworks via Halogenation for Enhanced Photocatalytic Water Splitting. *Angew. Chem. Int. Ed.* **2020**, *59*, 16902–16909. [[CrossRef](#)]
61. Aitchison, M.; Sprick, R.S.; Cooper, A.I. Emulsion polymerization derived organic photocatalysts for improved light-driven hydrogen evolution. *J. Mater. Chem. A* **2019**, *7*, 2490–2496. [[CrossRef](#)]
62. Shu, C.; Han, C.; Yang, X.; Zhang, C.; Chen, Y.; Ren, S.; Wang, F.; Huang, F.; Jiang, J.-X. Boosting the Photocatalytic Hydrogen Evolution Activity for D- π -A Conjugated Microporous Polymers by Statistical Copolymerization. *Adv. Mater.* **2021**, *33*, 2008498. [[CrossRef](#)] [[PubMed](#)]
63. Zhang, X.-H.; Wang, X.-P.; Xiao, J.; Wang, S.-Y.; Huang, D.-K.; Ding, X.; Xiang, Y.-G.; Chen, H. Synthesis of 1,4-diethynylbenzene-based conjugated polymer photocatalysts and their enhanced visible/near-infrared-light-driven hydrogen production activity. *J. Catal.* **2017**, *350*, 64–71. [[CrossRef](#)]
64. Dai, C.; Xu, S.; Liu, W.; Gong, X.; Panahandeh-Fard, M.; Liu, Z.; Zhang, D.; Xue, C.; Loh, K.P.; Liu, B. Dibenzothiophene-S,S-Dioxide-Based Conjugated Polymers: Highly Efficient Photocatalysts for Hydrogen Production from Water under Visible Light. *Small* **2018**, *14*, 1801839. [[CrossRef](#)] [[PubMed](#)]
65. Sachs, M.; Sprick, R.S.; Pearce, D.; Hillman, S.A.J.; Monti, A.; Guilbert, A.A.Y.; Brownbill, N.J.; Dimitrov, S.; Shi, X.; Blanc, F.; et al. Understanding structure-activity relationships in linear polymer photocatalysts for hydrogen evolution. *Nat. Commun.* **2018**, *9*, 4968. [[CrossRef](#)] [[PubMed](#)]
66. Sprick, R.S.; Jiang, J.X.; Bonillo, B.; Ren, S.; Ratvijitvech, T.; Guiglion, P.; Zwijnenburg, M.A.; Adams, D.J.; Cooper, A.I. Tunable organic photocatalysts for visible-light-driven hydrogen evolution. *J. Am. Chem. Soc.* **2015**, *137*, 3265–3270. [[CrossRef](#)] [[PubMed](#)]
67. Honda, Y.; Watanabe, M.; Hagiwara, H.; Ida, S.; Ishihara, T. Inorganic/whole-cell biohybrid photocatalyst for highly efficient hydrogen production from water. *Appl. Catal. B Environ.* **2017**, *210*, 400–406. [[CrossRef](#)]
68. Peng, Q.-X.; Xue, D.; Zhan, S.-Z.; Ni, C.-L. Visible-light-driven photocatalytic system based on a nickel complex over CdS materials for hydrogen production from water. *Appl. Catal. B Environ.* **2017**, *219*, 353–361. [[CrossRef](#)]
69. Wang, X.; Chen, B.; Dong, W.; Zhang, X.; Li, Z.; Xiang, Y.; Chen, H. Hydrophilicity-Controlled Conjugated Microporous Polymers for Enhanced Visible-Light-Driven Photocatalytic H₂ Evolution. *Macromol. Rapid Commun.* **2019**, *40*, 1800494. [[CrossRef](#)]
70. Wang, Z.; Mao, N.; Zhao, Y.; Yang, T.; Wang, F.; Jiang, J.-X. Building an electron push–pull system of linear conjugated polymers for improving photocatalytic hydrogen evolution efficiency. *Polym. Bull.* **2018**, *76*, 3195–3206. [[CrossRef](#)]
71. Liu, G.; Wang, T.; Zhang, H.; Meng, X.; Hao, D.; Chang, K.; Li, P.; Kako, T.; Ye, J. Nature-Inspired Environmental “Phosphorylation” Boosts Photocatalytic H₂ Production over Carbon Nitride Nanosheets under Visible-Light Irradiation. *Angew. Chem. Int. Ed.* **2015**, *54*, 13561–13565. [[CrossRef](#)] [[PubMed](#)]

Disclaimer/Publisher’s Note: The statements, opinions and data contained in all publications are solely those of the individual author(s) and contributor(s) and not of MDPI and/or the editor(s). MDPI and/or the editor(s) disclaim responsibility for any injury to people or property resulting from any ideas, methods, instructions or products referred to in the content.